Materials Science & Engineering A 850 (2022) 143409

Contents lists available at ScienceDirect

Materials Science & Engineering A

journal homepage: www.elsevier.com/locate/msea

Influence of particle content on the ductility of extruded non-recrystallized aluminium alloys subjected to shear loading

Asle Joachim Tomstad [a,*], Bjørn Håkon Frodal [b], Tore Børvik [a,b], Odd Sture Hopperstad [a,b]

[a] Structural Impact Laboratory (SIMLab), Department of Structural Engineering, NTNU – Norwegian University of Science and Technology, Trondheim, Norway
[b] Centre for Advanced Structural Analysis (CASA), NTNU, Trondheim, Norway

ARTICLE INFO

Keywords:
Aluminium
Constituent particles
Shear
Experimental-numerical approach
Anisotropy

ABSTRACT

In-plane shear tests were conducted on two extruded 6000-series aluminium alloys to investigate the influence of constituent particles on ductile fracture. The two alloys have previously been characterized and found to have different area fraction of constituent particles while having similar grain structure, crystallographic texture, strength, and work hardening. Specimens of both alloys were machined from flat profiles with their gauge section oriented along either the extrusion direction or the transverse direction. The specimens were loaded in shear until fracture and an experimental-numerical approach was employed to analyse the stress and strain fields, which involved digital image correlation and crystal plasticity finite element analysis. The fracture mode was determined by examining digital images captured during the experiment, while the fracture surface of representative specimens was examined in a scanning electron microscope. The shear strain across the gauge section at failure was substantially lower for the alloy with higher fraction of constituent particles, and the negative effect of the particle content on the ductility was found to be more pronounced for the tests in the transverse direction. The crystal plasticity finite element analyses showed an extensive texture development within the gauge region and that the local shear strain at failure was somewhat different in the two loading directions.

1. Introduction

Accurate prediction of fracture is crucial in the design of structural components subjected to mechanical loads. Aluminium alloys are appreciated for their good corrosion resistance, high strength-to-weight ratio, and excellent formability, and are versatile engineering materials with a wide range of structural applications. However, understanding the underlying mechanisms of ductile fracture is key to utilize the structural material to its full potential and to develop more accurate numerical tools.

Ductile fracture of aluminium alloys occurs due to the continuous process of nucleation, growth, and coalescence of voids [1,2]. Plastic straining and stress triaxiality govern the void growth [3,4]. The stress state and the direction of the loading with respect to the particle orientation affect the nucleation of new voids [5,6], while anisotropic plastic flow of the matrix material causes anisotropic void growth [7]. Void deformation, such as void distortion, occurs at low stress triaxiality [6], and sometimes the deformation of voids is constrained by embedded constituent particles by the void locking phenomenon [7,8]. The void coalescence mechanisms depend upon the stress triaxiality [7], the void spacing and relative position, and the nucleation of secondary voids [9,10].

Tension-torsion tests show that the shear stress state in pure torsion results in substantial plastic straining before fracture [11–15], and logarithmic fracture strains as high as 2 have been reported for shear specimens using grain-based strain estimates [16]. Several authors have previously investigated the shear ductility of textured aluminium alloys and report anisotropy in the fracture strain [17–22]. In Ref. [17], it was concluded that accounting for texture development is particularly important in shear. Damage quantification of specimens subjected to shear has been performed by post-mortem scanning electron microscopy [16] and in-situ laminography [23,24]. In Ref. [23], it was found that the growth of voids in shear occurred in the direction of the maximum strain, while in Ref. [24] particle cracking normal to the maximum stress direction was observed. The latter study also provides additional significant findings, as the void growth was constrained to the voids nucleated from particles, while pre-existing pores experienced closing. This finding emphasizes the importance of the constituent particle

* Corresponding author.
E-mail address: asle.joachim.tomstad@sintef.no (A.J. Tomstad).

https://doi.org/10.1016/j.msea.2022.143409
Received 22 February 2022; Received in revised form 3 June 2022; Accepted 4 June 2022
Available online 9 June 2022

population upon ductile shear fracture.

The influence of particle clusters on tensile ductility was investigated by Refs. [25–27], and in Ref. [27], anisotropy in the coalescence of voids was observed. The effect of the constituent particle population on the tensile ductility of isotropic and anisotropic aluminium alloys was investigated in Ref. [28]. The results showed a marked negative effect on the tensile ductility of a larger area fraction of constituent particles, and further the size distribution of the constituent particles and particle clustering were found to be important. The influence of the constituent particle population on the ductility of isotropic aluminium alloys was further investigated for moderate to low stress triaxialities by tension-torsion tests on a single notched tube specimen [15]. The results were unanimous with regards to the detrimental effect of an increased area fraction of constituent particles.

The extrusion process reduces the size and redistributes the constituent particle population as well as changing the texture of the material and has previously been found to be beneficial for the ductility in tension [28]. The present study aims to investigate the significance of the constituent particle population on the ductility in shear of two extruded 6000-series aluminium alloys. The alloys have different volume fractions of constituent particles, while having similar flow stress, grain structure and crystallographic texture. Shear specimens of both alloys were machined along the extrusion direction (ED) and the transverse direction (TD) of the extruded profile and tested in an in-house shear rig. The specimens were designed with regards to an experimental-numerical approach, which is inspired by Refs. [29,30]. Digital cameras and digital image correlation (DIC) analysis were used to obtain the displacement of the specimen's gauge section. Finite element models were made of the specimens, and simulations of the tests were run with boundary conditions found from the DIC analysis. A crystal plasticity model was used to accurately model the extruded material and thus to predict the stress and strain fields within the shear zone. Two specimens for each alloy, one in each of the tested material directions, were examined post-mortem in a scanning electron microscope (SEM).

The experiments revealed a significant influence of the constituent particle population on the shear ductility, and a lower bound estimate of the difference in ductility was established, as the alloy with the least amount of constituent particles experienced cracks which nucleated at the edge for some of the specimens. For the alloy with the lowest volume fraction of constituent particles, the shear strain at failure was markedly higher in test along TD, while no significant difference between the two material directions was found for the alloy with the highest volume fraction. However, the crystal plasticity simulations did indicate anisotropy at a microscopic level for both alloys. The crystal plasticity finite element analyses showed significant changes in the crystallographic texture during shearing which was dependent on the loading direction. This finding highlights the importance of including texture development in the modelling of materials subjected to large deformations in shear.

2. Materials and methods

2.1. Aluminium alloys

Two aluminium alloys, denoted 6110A and 6110B, of the 6000-series are investigated in this study and their chemical compositions are given in Table 1. These alloys have previously been characterized by Tomstad et al. [28]. While 6110A is an engineering alloy, 6110B is a tailored alloy, which was made to have similar grain structure, crystallographic texture, strength, and work hardening as 6110A but with a substantially higher volume fraction of constituent particles. These characteristics of 6110B were achieved by increasing the iron (Fe) and silicon (Si) content, as seen in Table 1. Both alloys contain dispersoids and have a non-recrystallized, fibrous grain structure. For simplicity, the alloys will henceforth be referred to as alloy A and alloy B.

The materials were delivered as homogenized DC-cast extrusion billets and then extruded into flat profiles with 40 mm width and 6 mm thickness. During homogenization, the materials were heated to 575 °C with a rate of 200 °C/h. After a holding time of 135 min, the materials were cooled to room temperature with a rate of −400 °C/h. The DC-cast extrusion billets were solutionized at 560 °C, with a holding time of 10 min. The billets were then chilled to 500 °C and mounted in a vertical extrusion press and extruded. The materials were water quenched immediately after extrusion and stretched 0.5%. The extruded profiles were then stored for 48 h at room temperature, before artificially aged to peak strength (temper T6) by heating to 185 °C with a rate of 200 °C/h. After a holding time of 8 h at 185 °C, the extruded profiles were air cooled to room temperature. More details about the extrusion process and the heat treatment can be found in Refs. [31,32]. The extrusion, transverse and normal directions of the extruded profiles will be referred to as ED, TD and ND, respectively.

Fig. 1 displays some results from the materials characterization performed by Tomstad et al. [28]. Images of the grain structure in the ED-ND plane from an optical microscope (OM) are shown in Fig. 1a and Fig. 1b for alloys A and B, respectively, displaying the non-recrystallized microstructure with flat and elongated grains. Fig. 1c and Fig. 1d show SEM images of the constituent particles in the ED-ND plane for alloys A and B, respectively, where the clustering of the particles into stringers along the extrusion direction (ED) and the tendency of the major axis of the particles to align with the ED are evident. The size distribution of the constitutive particles is shown in Fig. 1e and Fig. 1f for alloys A and B, respectively. The particle size distribution is normalized with respect to the particle population and displays the accumulated area percentage of the respective bin. The bins span 0.25 μm intervals in equivalent diameter, which is defined as the diameter of a circle with the same area as the respective particle. The particle size distribution is quite similar for the two alloys, with a small shift towards larger constituent particles for alloy B.

Table 2 compiles some measurements from the microstructural characterization performed by Tomstad et al. [28], where D_{ND} and D_{TD} are the grain size along ND and TD, respectively, and f_p is the area fraction of constituent particles. Since the grains are severely elongated in the ED, as seen in Fig. 1a and Fig. 1b, no accurate measurement of the grain size in the ED was possible and is therefore not provided. It is apparent that alloy B has a very high area fraction of constituent particles, which is almost four times higher than that of alloy A.

Pole figures, representing the macroscopic crystallographic texture of the extruded profiles, were extracted with a Siemens D5000 X-ray diffractometer. Samples were cut from the extruded profile, ground down to the centre of the profile, etched for 10 min with Alubeis and further etched with HNO_3 for 20–30 s [31]. The pole figures were constructed using cubic crystal symmetry and triclinic sample symmetry [33]. The measured crystallographic texture of the alloy A and alloy B is shown in Fig. 2a, and Fig. 2b, respectively. Fig. 2c displays the crystallographic texture applied in the subsequent CP-FEM simulations. The texture can be described as a cube texture with orientations along the β-fibre, which is typical for non-recrystallized aluminium alloys with

Table 1
Chemical composition of the aluminium alloys in wt-%.

Alloy	Mg	Si	Fe	Cu	Mn	Zn	Ti	Cr	Al
A	0.828	0.720	0.196	0.203	0.506	0.003	0.026	0.157	Bal.
B	0.793	0.925	0.749	0.204	0.503	0.005	0.029	0.183	Bal.

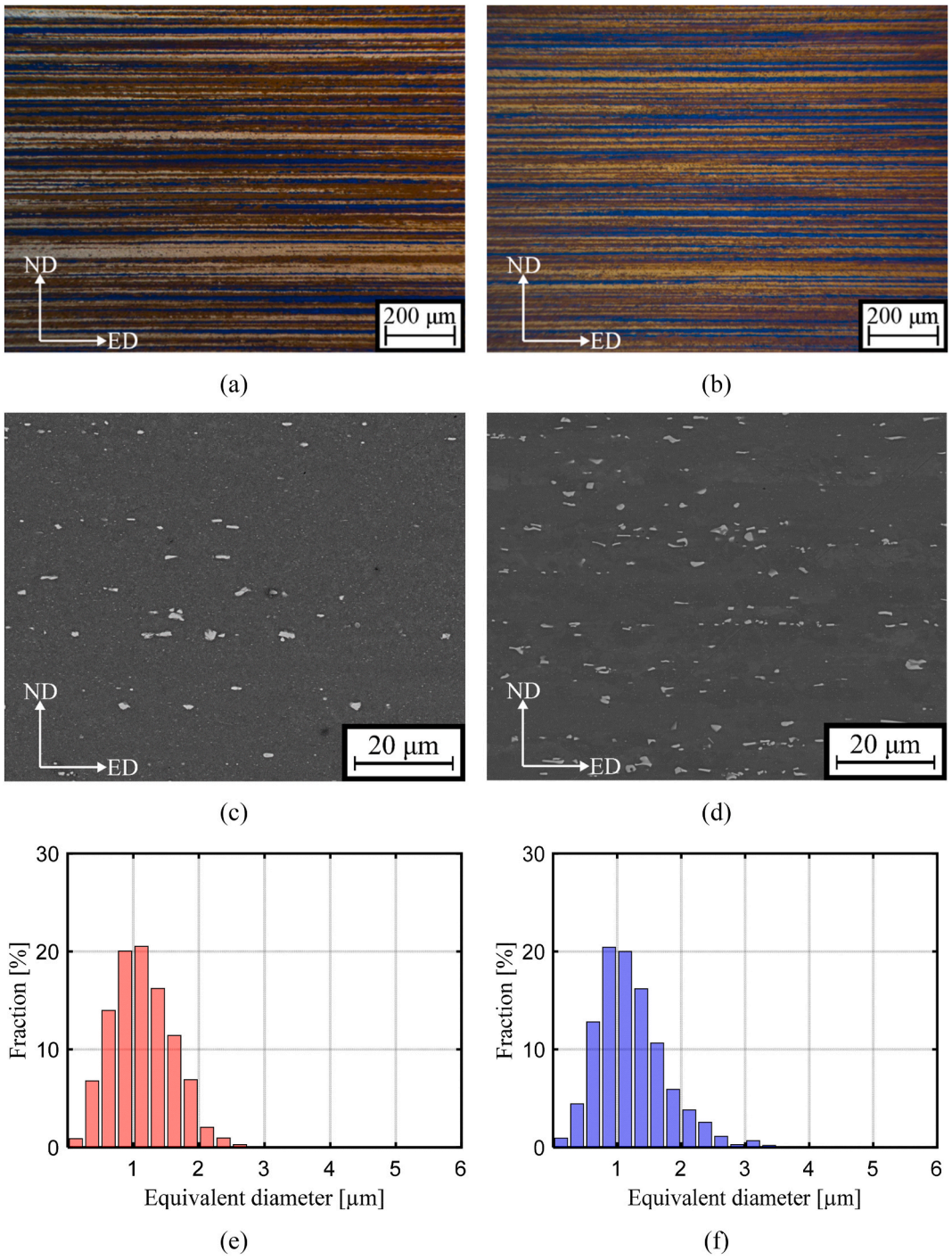

Fig. 1. Selected results from the materials characterization: (a) grain structure in the ED-ND plane of alloy A, (b) grain structure in the ED-ND plane of alloy B, (c) constituent particles in the ED-ND plane of alloy A, (d) constituent particles in the ED-ND plane of alloy B, (d) particle size distribution of alloy A, and (e) particle size distribution of alloy B.

Table 2
Selected microstructural quantities of the alloys.

Alloy	D_{ND} [µm]	D_{TD} [µm]	f_p [–]
A	4	8	0.0079
B	3	6	0.0301

fibrous grain structure [34], and was the same for the two alloys.

Fig. 3 displays the stress-strain curves for the two alloys in terms of the true stress and the logarithmic strain. The data was adapted from Tomstad et al. [28], and here the red curves correspond to alloy A, while the blue curves correspond to alloy B. Tensile tests were performed in the ED and TD, and excellent agreement between the flow stress of alloys A and B is evident in both directions. The curves are plotted to failure, defined as the point where the true stress reaches its maximum value. Note that the stress is not corrected for structural effects induced by diffuse necking.

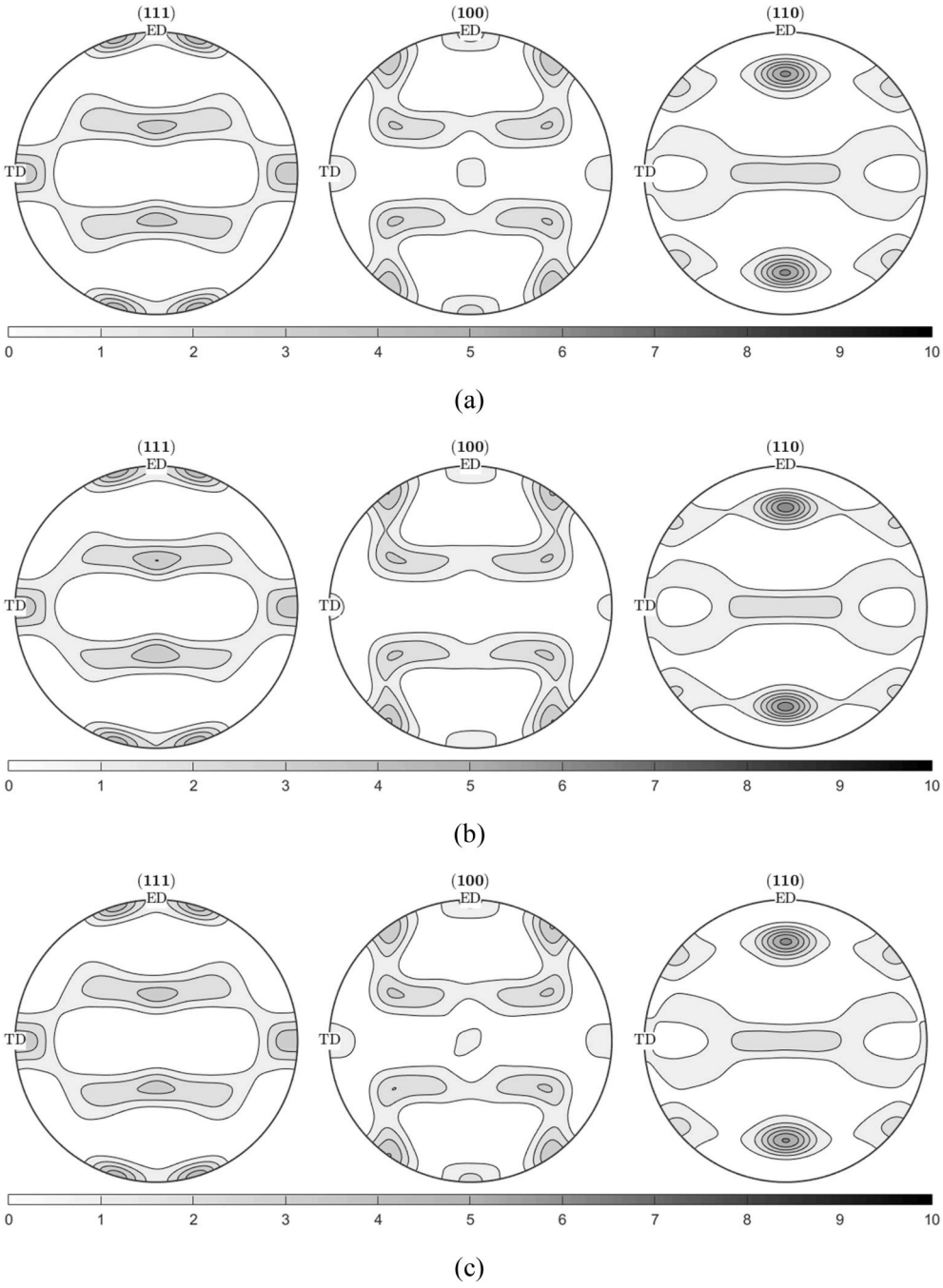

Fig. 2. Initial crystallographic texture represented by (111), (100) and (110) pole figures: (a) alloy A, (b) alloy B, and (c) applied in the CP-FEM simulations.

2.2. Mechanical test programme

2.2.1. Specimen and mechanical test setup

The geometry of the shear specimen used in this study is based on the geometry proposed in Ref. [35], and a detailed drawing is provided in Fig. 4. The specimens were machined from the 6 mm thick and 40 mm wide extruded profiles with the loading direction either along ED or TD. In Fig. 4, the loading direction is vertical. The specimen was made by first milling down the thickness to 4 mm, followed by electrical discharge machining of the final geometry. Sixteen specimens were made for this study, i.e., eight specimens per alloy. The first four specimens of each alloy were machined with the groove aligned with TD, and the latter four with the groove aligned with ED. The specimens are denoted A1 to A8 and B1 to B8 for alloys A and B, respectively.

The test setup used to perform the shear tests is shown in Fig. 5. The specimens were mounted in a shear test apparatus, which was installed in an Instron 5982 universal testing machine with a 100 kN load cell. The shear test apparatus or "shear device" consists of a stationary part which is bolted onto the universal testing machine, while the actuator of the shear device glides in a well lubricated rail with ball bearings. The actuator is connected to the crossbar of the universal testing machine. Two Basler acA4112-30um digital cameras were used to capture the deformation of the specimen, with a resolution of 4096 $\times$ 2000 pixels. In a test, the left-hand side of the shear specimen is fixed, while the right-hand side is displaced vertically with a speed of 0.6 mm/min by the actuator.

Digital image correlation (DIC) was applied to measure the deformation of the specimen, using the in-house DIC-code eCorr, see Ref. [36]

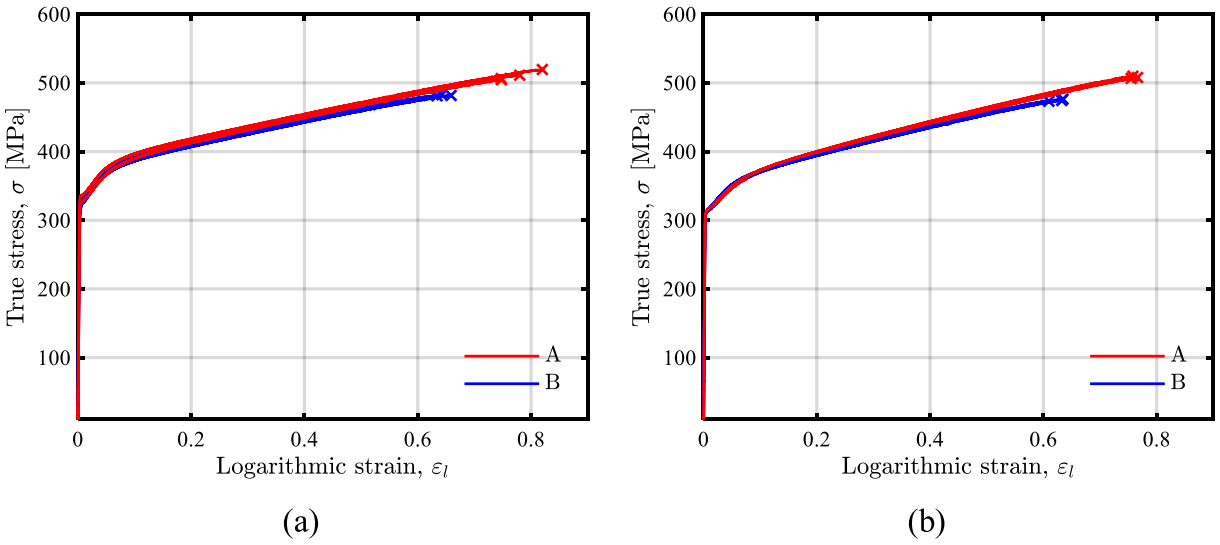

Fig. 3. Stress-strain curves of the two 6110 alloys in two directions: (a) ED and (b) TD, where the onset of failure is indicated by the markers.

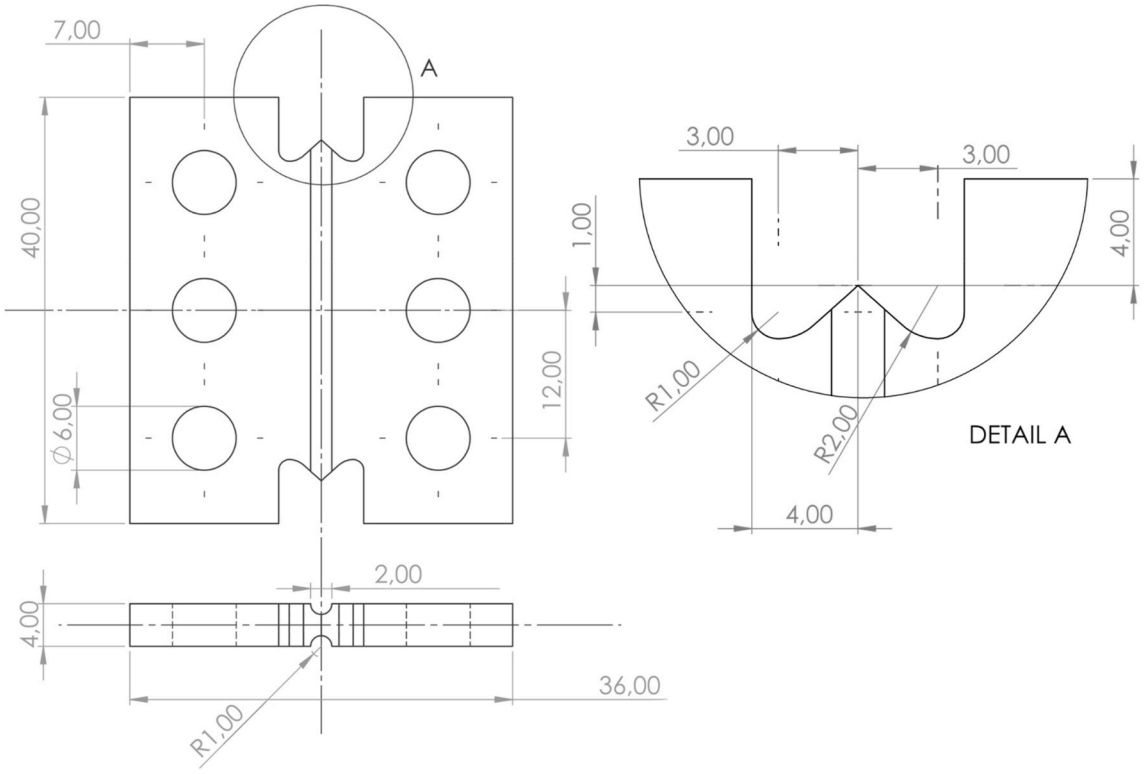

Fig. 4. Geometry of shear specimen (measures in mm).

for details. The specimens were painted with a speckle pattern for the DIC mesh on one side and black on the opposite side to assist the determination of the crack propagation. A frequency of 4 Hz was used for the cameras, which were synchronized with the force measurements of the testing machine's load cell. The DIC mesh is described in detail in Section 2.2.2.

2.2.2. *Mechanical test analysis*

Fig. 6 shows a close-up of the gauge region of the shear specimen with the DIC mesh superimposed. The global coordinate system *XY* is shown in the lower left corner, where the *X*-axis is aligned with the loading direction, while the *Y*-axis is aligned with the transverse direction of the specimen. In Fig. 6, the lower part of the specimen is mounted to the actuator while the upper part is fixed. The DIC mesh of the upper and lower part of the specimen was made in Abaqus/CAE [37] and imported into eCorr. The mesh was designed such that an element covers 25 × 25 pixels. There is a 0.16 mm gap between the groove and the mesh on either side, and a 0.23 mm gap between the mesh and the left and right edges of the specimen. Some small discrepancies in the gaps were accepted, due to the tolerances and alignment of the specimen. The mesh slants inwards when approaching the groove to prevent early termination of the DIC analysis due to large element distortion.

The displacements of the specimen in the *X*- and *Y*-directions were extracted in the three points marked on the upper and lower green

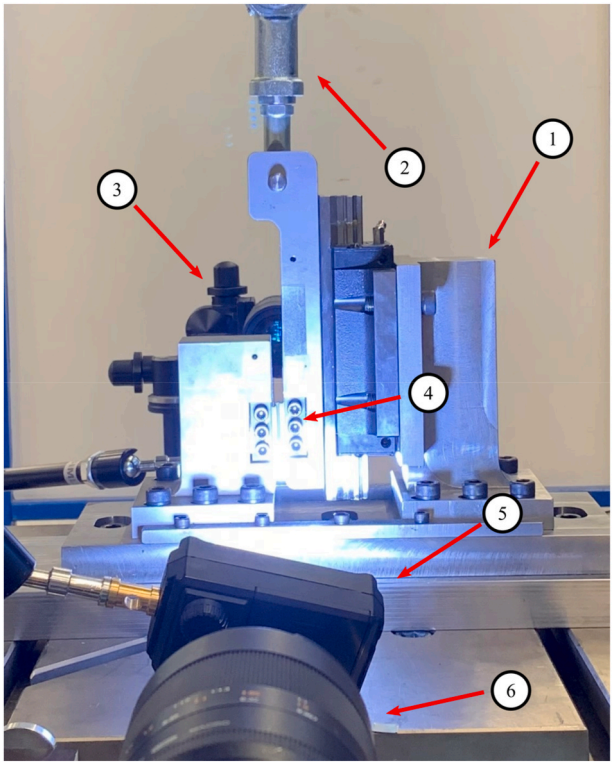

Fig. 5. Test setup applied for shear testing, including (1) the shear test apparatus, (2) the universal testing machine, (3) the backside camera, (4) the specimen mounted in the shear test apparatus, (5) one of the two light sources, and (6) the frontside camera.

horizontal lines drawn on the specimen in Fig. 6. These points are the two end points and the mid-point of the lines. The lines are located 3.19 mm from the centre of the specimen in the Y-direction. A local corotational coordinate system $\overline{xy}$ is fixed to the upper middle node, which was used to determine the boundary conditions of the finite element model described in Section 2.3. The local coordinate system rotates along with the small rotation of the upper line. It is assumed that the upper and lower lines are subjected to rigid body motion, which was supported by the measurements. The displacements were logged in pixels, and the conversion from pixels to mm was done by use of the nominal distance between the two tips in the gauge area. These points vary very little between the specimens and the distance is sufficiently large (32 mm) as to prevent major errors in the conversion. As an example, an error of ± 1 mm in this distance will introduce less than 4% error in the conversion.

Five virtual strain gauges are evenly distributed along the gauge length and measure the shear strain as the angle change between two lines initially parallel with the X- and Y-axes, see Fig. 6. The measurements from the virtual strain gauges were used to calculate the average shear strain across the groove.

2.3. Numerical analysis

A finite element (FE) model of the shear specimen was established and used to simulate the experimental tests. These simulations provide estimates of the local stress and strain fields and the texture evolution within the groove of the shear specimen. The finite element model was made in Abaqus/CAE and consisted of the central part of the specimen between the upper and lower lines in Fig. 6, with symmetry boundary conditions along the ED-TD midplane. The nominal geometry of the specimen was used in the modelling. Linear hexahedral elements with selectively reduced integration (element type C3D8 in Abaqus) were used with a characteristic element size of 50 μm, and the final mesh consisted of 1.83 million elements. The nodes along the upper and lower lines were constrained to the nodes in the mid-points of the upper and lower lines using a beam constraint. The upper middle node was pinned, while boundary conditions were applied to the degrees of freedom u, v and θ of the lower middle node, see Fig. 6. The boundary conditions were determined from the experimental DIC measurements such that the finite element model followed the same relative displacement of the upper and lower lines. A rate-dependent single crystal plasticity model was used in the numerical simulations, i.e., the crystal plasticity finite element method (CP-FEM) was adopted. The element size was selected to give sufficiently accurate estimates of the stress and strain fields while maintaining a reasonable computational time. Each element was assumed to be an individual grain and given an initial orientation such that the macroscopic texture of the finite element model was in accordance with the measured crystallographic texture of the alloys. However, the fibrous grain structure of the alloys was not accounted for in the model, given that the elements are nearly cubical. Notwithstanding, the heterogeneity introduced by the grains of different orientation is represented in some sense by the FE model, and the approach allows for simulating the texture development during straining. The CP-FEM simulations were conducted in Abaqus/Explicit with a uniform mass-scaling factor of $4{\cdot}10^{10}$, and a simulation time of $\sim$ 300s. Using 48 AMD EPYC 7352 CPU cores, this resulted in a computational time of roughly two weeks. It was checked that the kinetic energy remained small compared to the internal energy throughout the deformation process and the simulations could therefore be characterized as quasi-static.

2.3.1. Single crystal plasticity

A rate-dependent single crystal plasticity model was used in the finite

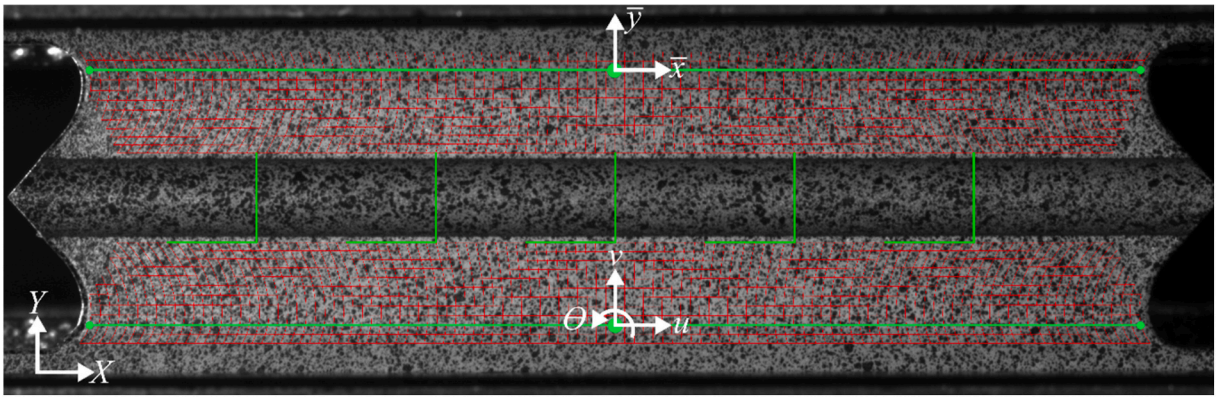

Fig. 6. Specimen with DIC mesh superimposed where virtual points and lines used to measure displacement and rotation, and virtual strain gauges used to measure the shear strain are visualized.

element simulations. The model is based on a hypoelastic formulation of single crystal plasticity and allows for finite plastic deformations and rotations, but only small elastic deformations. The single crystal plasticity model has been implemented in Abaqus/Explicit as a user-material subroutine (VUMAT) and a detailed description of the model can be found in Ref. [38]. In the following, only the constitutive relations defining the plastic slip on the slip systems are summarized.

The plastic slip rate $\dot{\gamma}^{\alpha}$ on slip system α is defined by the viscoplastic relation

$$\dot{\gamma}^{\alpha} = \dot{\gamma}_0 \left| \frac{\tau^{\alpha}}{\tau_c^{\alpha}} \right|^{\frac{1}{m}} \mathrm{sgn}(\tau^{\alpha}) \tag{1}$$

where τ^{α} are the resolved shear stresses, τ_c^{α} are the critical resolved shear stresses, $\dot{\gamma}_0$ is the reference shearing rate, and m governs the rate sensitivity of the material. The critical resolved shear stress is defined by the evolution equation

$$\dot{\tau}_c^{\alpha} = \theta(\Gamma) \sum_{\beta=1}^{N} q_{\alpha\beta} \left| \dot{\gamma}^{\beta} \right| \tag{2}$$

where $q_{\alpha\beta}$ is the latent hardening matrix and N is the number of slip systems, which equals 12 for aluminium alloys. The initial value of the critical resolved shear stress is the same for all slip systems and set equal to τ_0. The work hardening rate $\theta(\Gamma)$ depends upon the accumulated plastic shear strain Γ, and it is defined by

$$\theta(\Gamma) = \sum_{k=1}^{N_\tau} \theta_k \exp\left(-\frac{\theta_k}{\tau_k} \Gamma \right) \tag{3}$$

where N_τ is the number of hardening terms, and θ_k and τ_k are the initial hardening rate and the saturated value of the hardening term k, respectively. The accumulated plastic shear strain is given as

$$\Gamma = \int_0^t \sum_{\alpha=1}^{N} |\dot{\gamma}^{\alpha}| dt \tag{4}$$

To provide a scalar measurement of the plastic deformation, the von Mises equivalent plastic strain, ε_{eq}^{p}, defined as

$$\varepsilon_{eq}^{p} = \int_0^t \sqrt{\frac{2}{3} D_{ij}^{p} D_{ij}^{p}} dt \tag{5}$$

was employed, where D_{ij}^{p} is the plastic rate-of-deformation tensor.

As the strength, work hardening and crystallographic texture of alloys A and B are similar, only simulations with parameters calibrated for alloy A were conducted. The material model parameters, obtained in Ref. [39], are provided in Table 3. Simulations were performed with the loading along the ED and TD in a similar way as in the experiments.

3. Results and discussion

The experimental and numerical force-displacement curves are plotted in Fig. 7 with loading along ED and TD. The point at maximum force is defined as the point of failure. At this point the specimens develop the crack that eventually leads to total failure of the specimen.

Table 3
Material model parameters (from Ref. [39]).

C_{11} (MPa)	C_{12} (MPa)	C_{44} (MPa)	ρ (kg/m^3)	$q_{\alpha\beta}$	$\dot{\gamma}_0$ (s^{-1})
106430	60350	28210	2700	1.0 if $\alpha = \beta$ 1.4 if $\alpha \neq \beta$	0.01
m	τ_0 (MPa)	θ_1 (MPa)	τ_1 (MPa)	θ_2 (MPa)	τ_2 (MPa)
0.005	96.9	177.4	21.3	3.2	$3.5{\cdot}10^6$

The experimental force and displacement are measured along the global X- coordinate, while in the CP-FEM simulations these quantities are measured in the corotated local $\bar{x}$-coordinate. The rotation of the local coordinate system stays below 2° during the entire course of deformation, and the discrepancy caused by a different frame of reference is deemed insignificant.

The difference in the force level between tests on the A and B alloys is negligible for loading in TD, while there is a small but visible difference for loading in ED. The force level is quite similar in tests along ED and TD for the same alloy, but the tests in ED exhibit a slightly lower initial force level and a higher work-hardening at the later stages. The displacement at failure is clearly higher for alloy A than for alloy B, which is caused by the much higher area fraction of particles in alloy B. For alloy A, the displacement at failure is significantly larger in TD than in ED, while for alloy B, the difference in the two directions is insignificant. The mean force at failure is indistinguishable between the two directions for alloy A, while for alloy B the mean force at failure is 450 N higher in ED than in TD. One test of each combination of alloy and load direction was stopped just past failure and was saved for possible later examination. All tests show good repeatability, except for the tests of alloy B in ED, where there is some scatter in both the force level and the displacement at failure.

In the CP-FEM simulations, the elastic stiffness is overestimated, and the force level consistently underestimated in the plastic domain. These observations hold for both load cases. The overestimation of the elastic stiffness is likely caused by the boundary conditions being too stiff in the finite element model. Friction is likely a contributor to the higher force level in the experiments, despite utilizing lubricants to minimize friction in the actuator of the shear device. For both load cases, the maximum error in the predicted force level is 8%. The slope of the force-displacement curve in the plastic domain (essentially the work-hardening of the alloy) is well captured in the simulation of both load cases, even though it is somewhat overestimated at large displacement for loading along TD.

In Fig. 8, the shear strain-displacement curves are presented for all tests and simulations, where the shear strain, γ, is the average value of the five virtual strain gauges. It is evident that the shear strain-displacement curve is largely the same for the two alloys in both load cases, which is likely a result of the highly constrained plastic deformation within the groove of the shear specimens. Alloy B has a substantially lower average shear strain at failure compared with alloy A (in average 14% lower in ED and 22% lower in TD), and the failure strain is similar in the two load cases (in average 2.5% lower in TD than in ED). In contrast, the average shear strain at failure is considerably larger for loading along TD than along ED for alloy A (in average 7% higher in TD than in ED). The excellent agreement between the experimental and numerical shear strain-displacement curves provides credibility to the predicted deformation field within the gauge area. These results concur with previous experimental observations by Tomstad et al. [28], where a marked effect of the particle content on the tensile ductility of the same materials was found. Further, the recent work by Tancogne-Dejean et al. [24] indicates that the damage mechanisms active in shear are dependent upon the amount of constituent particles.

Fig. 9 and Fig. 10 show contour plots of the logarithmic shear strain, γ_{xy}, on the surface of the groove at failure in specimens loaded along ED and TD, respectively, obtained by DIC analysis of the experimental data and CP-FEM simulations. Only alloy B is addressed in these figures, as the DIC mesh became heavily distorted for alloy A at failure due to the high ductility. Note that the fields were assessed visually and may therefore be subjected to operator bias. The DIC analyses and CP-FEM simulations are in good agreement for both load cases. It is seen that the strain field from the CP-FEM simulations is heterogeneous because each element/grain has a distinct crystallographic orientation governed by the crystallographic texture. It should be noted that the resolution in the CP-FEM simulations is much higher than in the DIC analyses, which

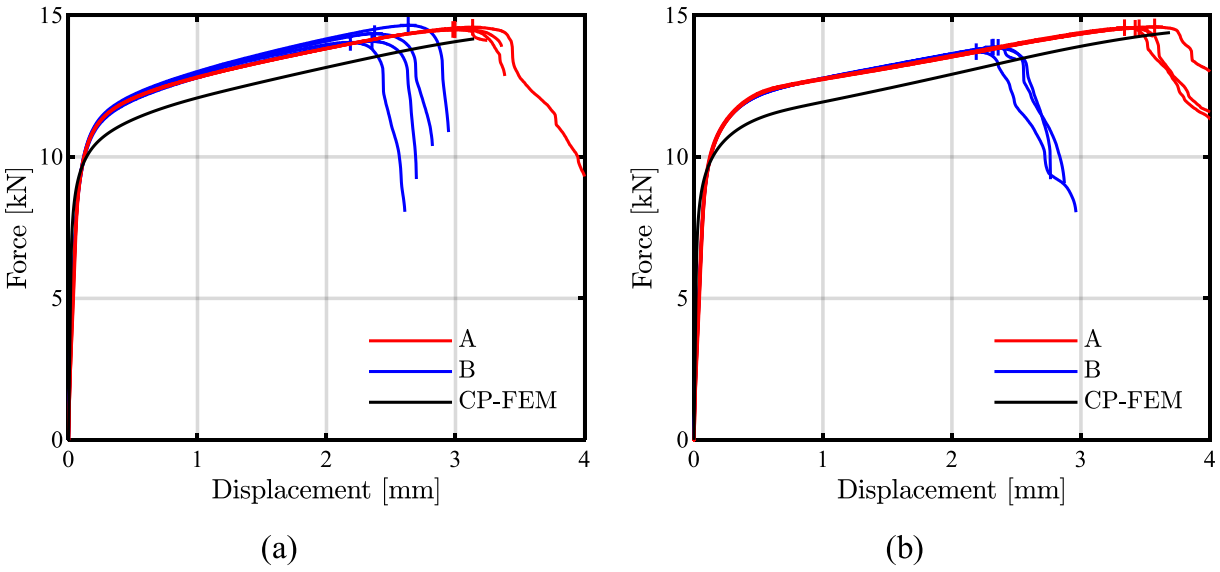

Fig. 7. Force-displacement curves for loading in (a) ED and (b) TD, where the failure is indicated by the markers.

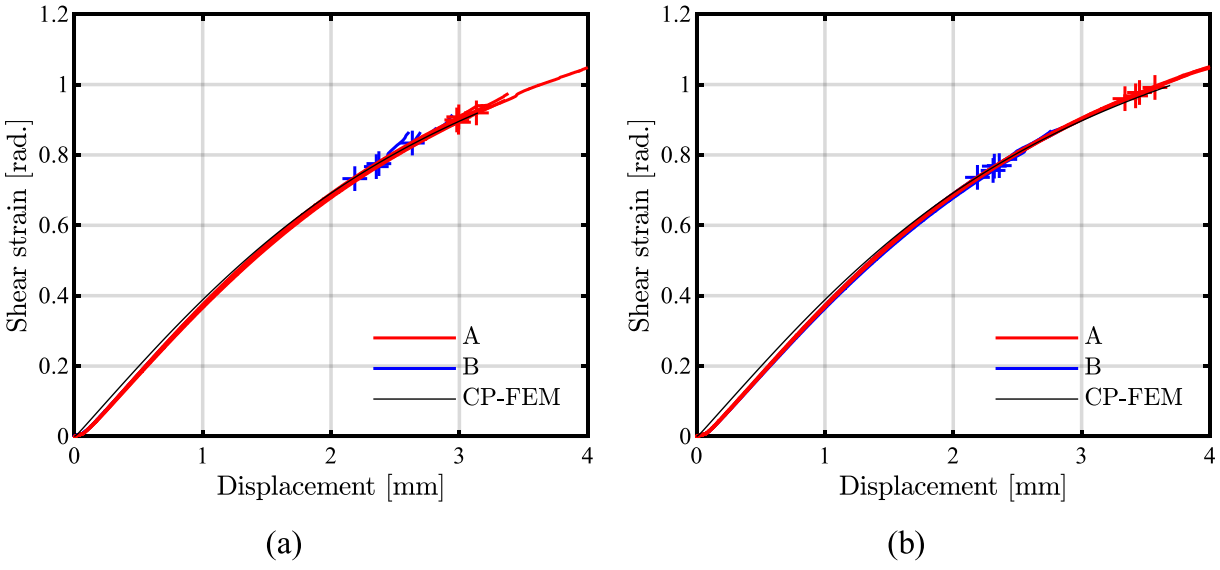

Fig. 8. Average shear strain-displacement curves for loading along (a) ED and (b) TD, where the failure is indicated by the markers.

influences the heterogeneity of the strain field. In both load cases, the measured logarithmic shear strain in the highly strained area of the groove spans from 1.2 to 1.5. In the CP-FEM simulations, the strain field is significantly more heterogeneous for loading along ED than along TD, which is likely caused by the strong deformation texture of the alloy. The predicted logarithmic shear strain in the highly strained area of the groove spans from 1.2 to 2.0 for loading along ED compared to 1.2 to 1.5 for loading along TD.

The von Mises equivalent plastic strain field on the surface of the groove in the CP-FEM simulations of the shear tests in the ED and TD is shown in Fig. 11. For each load case, the strain field is plotted at a displacement that is representative for the displacement at failure of alloy B. It appears that the highly strained zone is somewhat wider for loading along TD (Fig. 11b) than along ED (Fig. 11a). Inside this area, the strain level is between 1.5 and 2.0 for loading along ED and between 1.5 and 2.2 for loading along TD. This contrasts with Figs. 9b and 10b where the logarithmic shear strain, γ_{xy}, on the surface was higher for loading along ED than along TD, implying that other components of the plastic strain tensor are more prevalent for alloy B loaded along TD. Further straining to failure of alloy A causes widening and lengthening of the highly strained zone for both load cases. The difference in characteristics of the zones is retained, and the strain levels increase to between 1.9 and 2.7 in both load cases, with a slight bias towards the upper bound for loading along TD. Note that the strain fields were assessed visually and may thus be subjected to operator bias.

In both load cases, the von Mises equivalent plastic strain is significantly higher at the surface than in the interior of the specimen, while the stress field, evaluated in terms of the Lode parameter and the stress triaxiality, is rather uniform through the thickness. In both load cases the Lode parameter and the stress triaxiality were in the range 0 ± 0.4 and 0 ± 0.2, respectively, which shows that the gauge section is in a predominate shear stress state. Contour plots of the distribution of the Lode parameter and the stress triaxiality on the surface of the groove are provided in Figure A1 and Figure A2, respectively, in the Appendix.

The initial texture applied in the CP-FEM model is shown in Fig. 2c and is seen to compare well with the experimentally measured texture of the extruded profile. To assess the texture development during the deformation, the highly strained volume in the groove of the specimen

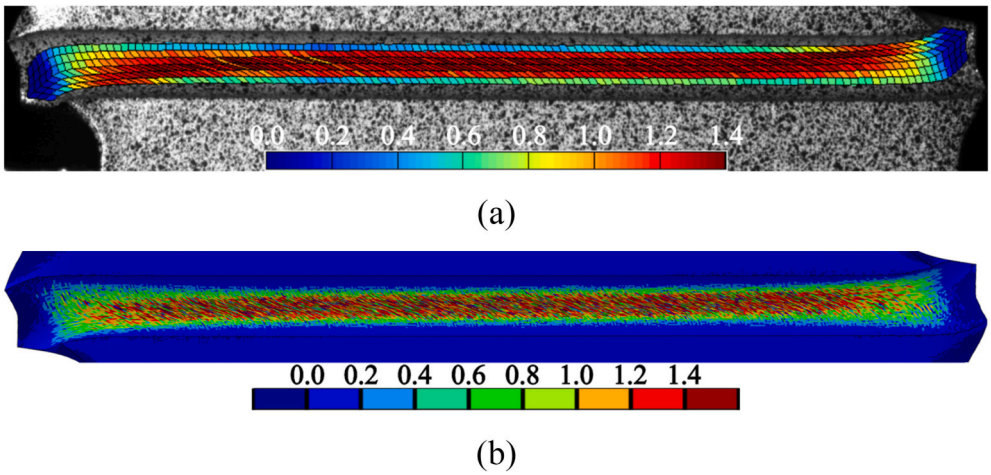

Fig. 9. Contour plot of the logarithmic shear strain, γ_{xy}, in the groove of the specimen at failure in the shear test of alloy B loaded in ED: (a) DIC analysis (specimen B7) and (b) CP-FEM simulation.

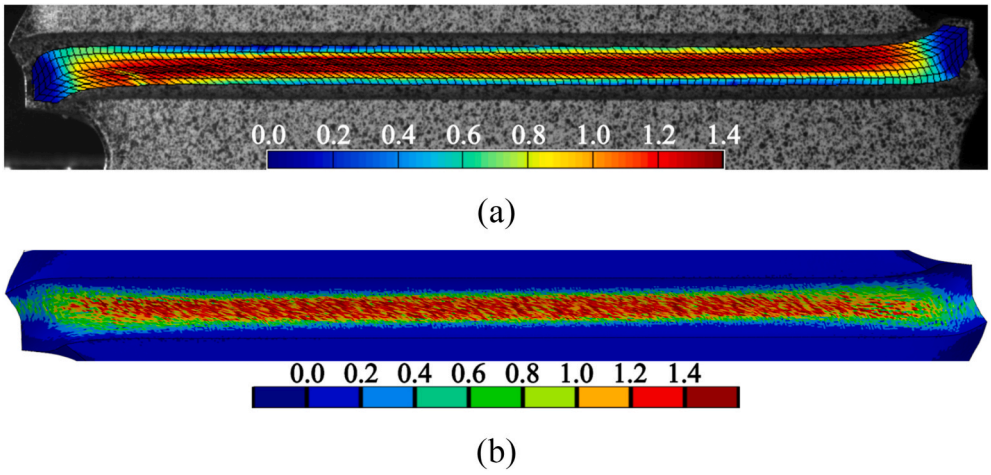

Fig. 10. Contour plot of the logarithmic shear strain, γ_{xy}, in the groove of the specimen at failure in the shear test of alloy B loaded in TD: (a) DIC analysis (specimen B4) and (b) CP-FEM simulation.

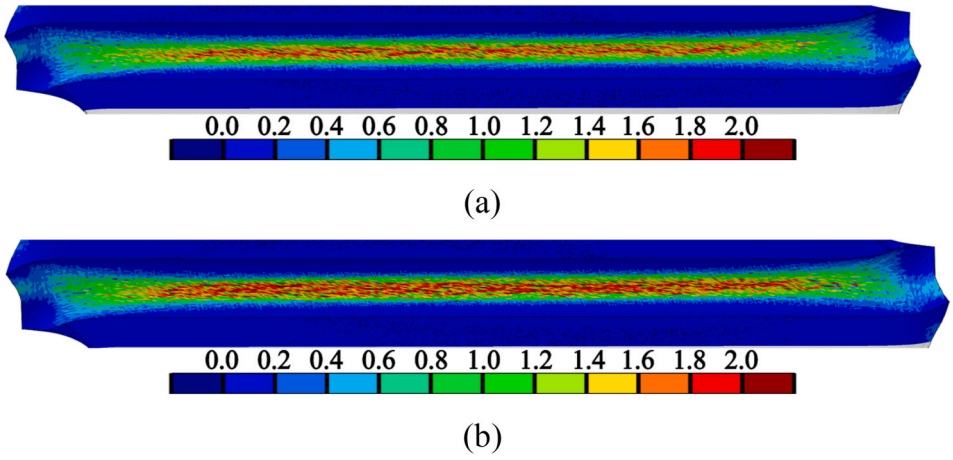

Fig. 11. Contour plots of the von Mises equivalent plastic strain on the surface of the grove in the CP-FEM simulations at a displacement corresponding to the displacement at failure for alloy B with loading in (a) ED and (b) TD.

was examined. The examined volume contained 28744 elements, and each individual integration point was interpreted as a unique data point. An Abaqus python script was used to extract the Bunge Euler angles (φ_1, Φ, φ_2) at given displacements of the specimen, and the pole figures were reconstructed with cubic crystal symmetry and triclinic sample symmetry. Fig. 12 shows the predicted texture of the deformed specimens in

simulations of the shear tests in the ED and TD. For each load case, the pole figures are plotted at a displacement that is representative for the displacement at failure of alloy B. When the loading is along ED, the initial deformation texture develops into a inverse Goss texture (Fig. 12a), while it develops into a Goss texture when the loading is along TD (Fig. 12b). In both load cases, the texture is shown at a strain corresponding to failure of alloy B. Further straining in the two material directions to the strain corresponding to failure of alloy A leads to strengthening of these textures. These findings underline the importance of accounting for the crystallographic texture and its evolution when analysing shear tests.

Typical crack propagation paths within the groove of the specimens are shown in Fig. 13 and Fig. 14 together with the force-displacement curve with markers that indicate at which displacement the images of the cracks were taken. These images were captured using the backside camera (see Fig. 5), and the groove on this side of the specimen was painted black to better accentuate the cracks. The crack path of specimen B4 is shown in Fig. 13, i.e., a specimen of alloy B loaded along TD. Fig. 13b shows an early edge crack, which was caused by a local tensile stress field at the edge [40]. This crack appeared around a displacement of 1.77 mm, and no visual impact of this crack on the force-displacement curve is found. The early edge crack was quickly arrested, likely by blunting of the crack tip, and did not propagate further into the specimen. A propagating crack nucleated in the highly strained area of the groove is shown in Fig. 13c. The propagating crack eventually reached the edges, see Fig. 13d, in this case avoiding the early edge crack, and ultimately caused total fracture of the specimen. In several specimens, final fracture occurred when the propagating crack coalesced with the early edge crack or coalesced with a subsequently nucleated crack, propagating from the location in Fig. 14c.

Some of the specimens of alloy A displayed a different crack path which is shown in Fig. 14 for specimen A4, i.e., a specimen of alloy A loaded in TD. Also in this specimen, an edge crack developed early in the deformation process but was arrested without propagating further into the groove, as shown in Fig. 14b. As also stated above, there is no visible effect on the force-displacement curve caused by the early edge crack. The crack that led to total failure nucleated on the edge at the opposite side of the groove (Fig. 14c), propagated inwards (Fig. 14d), and eventually merged with a crack propagating from the other side of the specimen. Visual inspection of the captured images provided credible evidence that all specimens of alloy B failed due to crack initiation within the highly strained area of the groove, while both types of crack paths were found for specimens of alloy A in both directions. The alternating failure mode observed for alloy A indicates that the specimens are either failing in shear or close to failing in shear. Thus, the failure strain obtained for alloy A can safely be considered a lower bound of the ductility in shear.

The fracture surfaces of four selected specimens, namely A4, B4, A6, and B6, were examined in the SEM. Specimens A4 and B4 were loaded along TD, while specimens A6 and B6 were loaded along ED. Typical features of the fracture surfaces are presented in Fig. 15. All images are oriented with the direction of straining horizontally and towards the right. Fig. 15a and Fig. 15b depict features associated with shear fracture, i.e., flat fracture surfaces with limited void growth. Fig. 15a

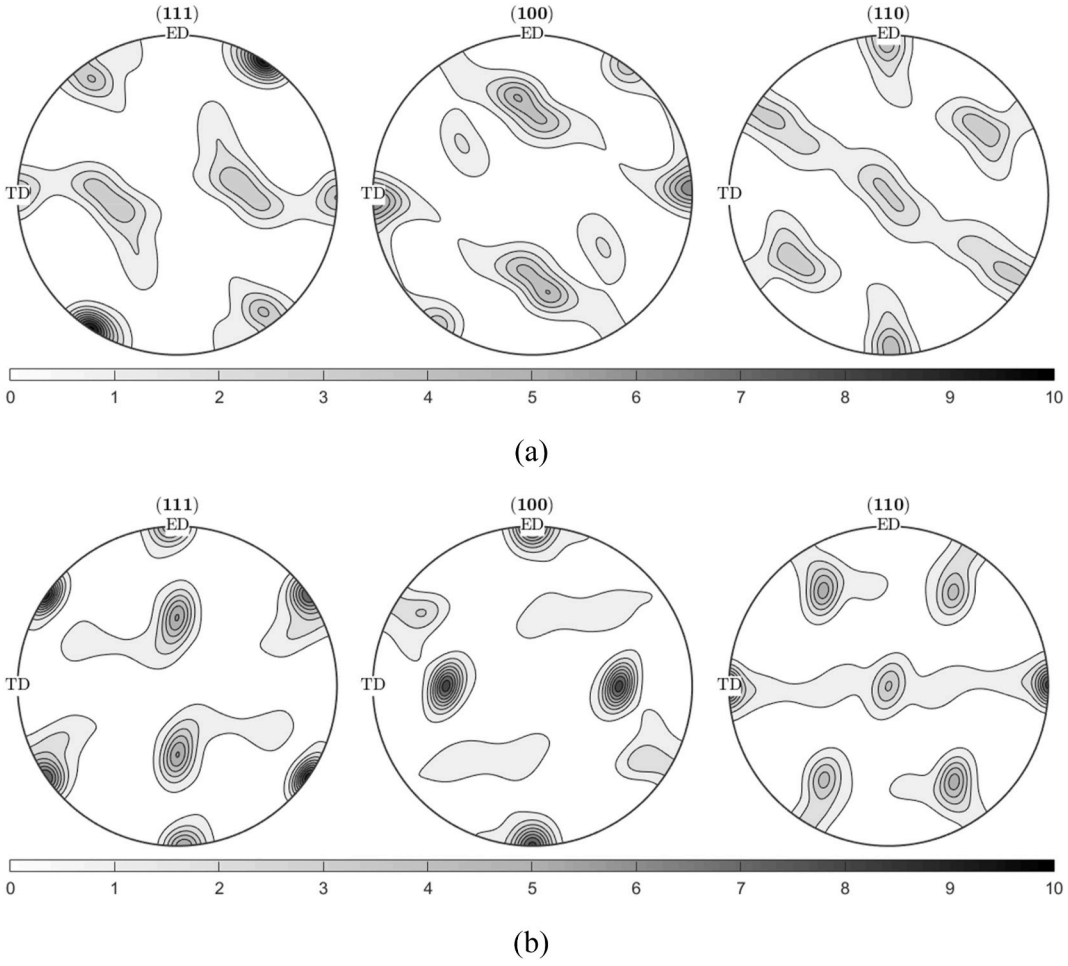

Fig. 12. Deformed texture represented by (111), (100) and (110) pole figures from CP-FEM simulations at a displacement corresponding to the displacement at failure in the test for alloy B with loading along (a) ED and (b) TD.

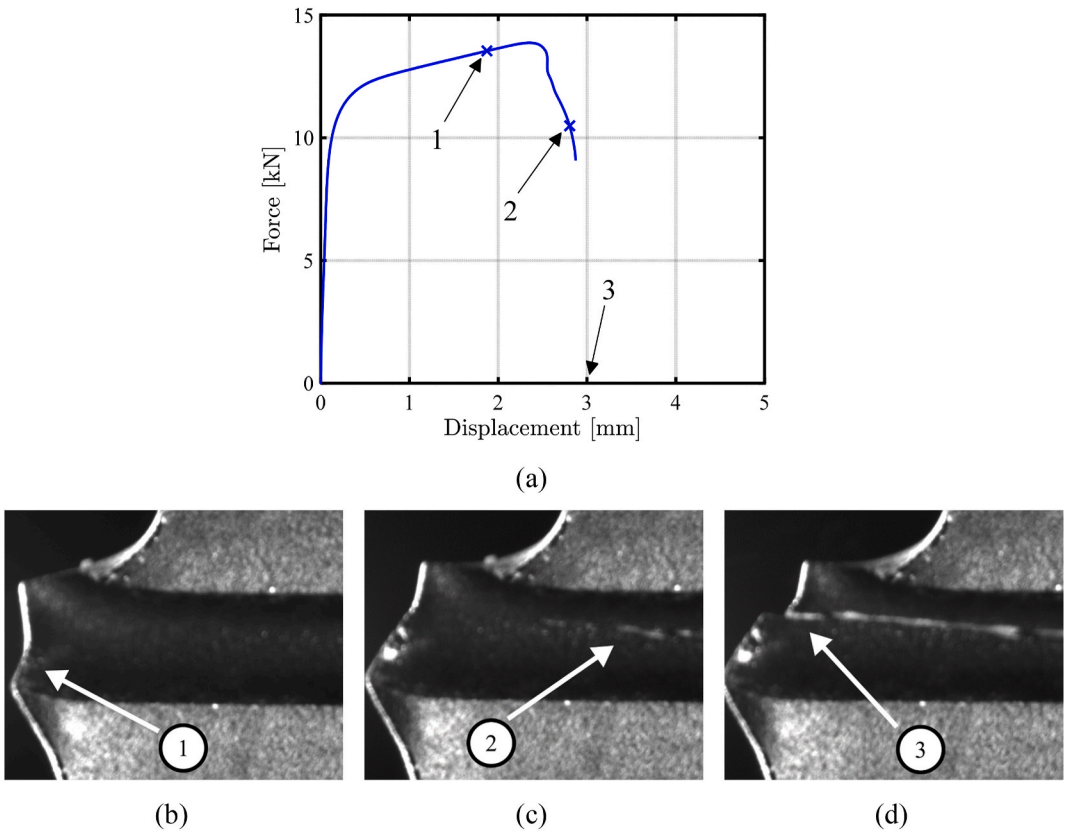

Fig. 13. Failure of specimen B4: (a) Force-displacement curve with annotations, (b) early edge crack, (c) crack propagation and (d) total failure.

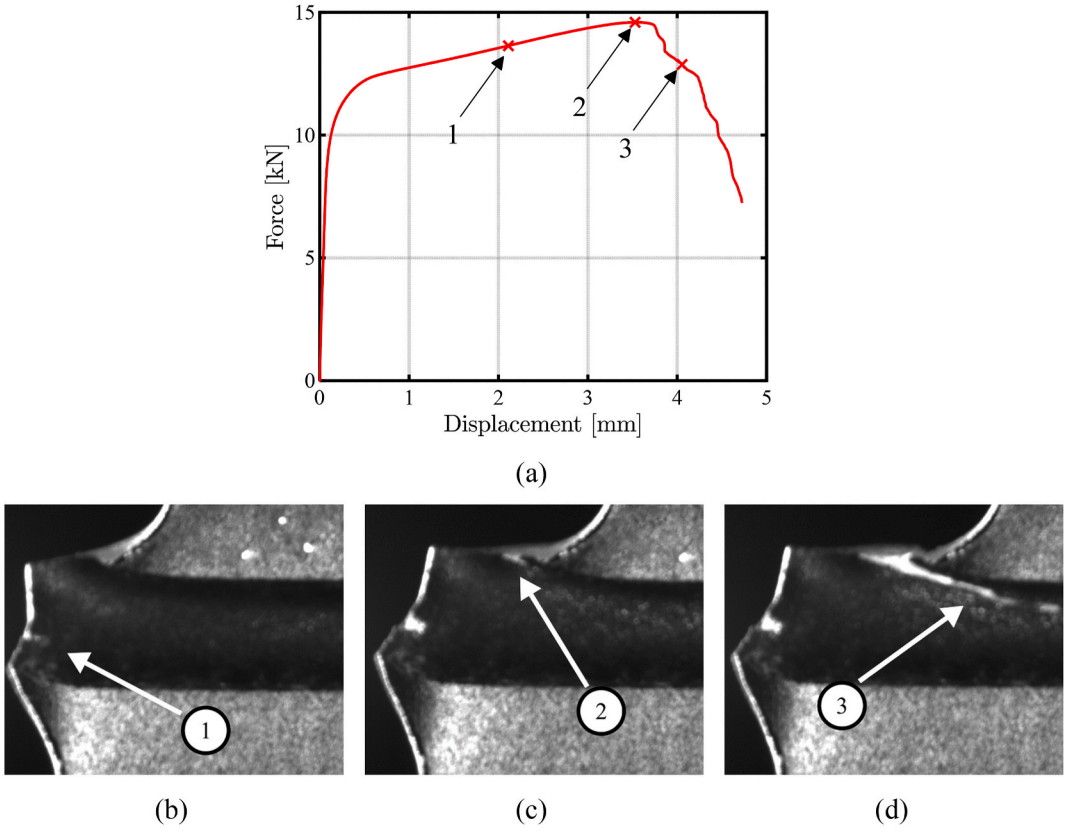

Fig. 14. Failure of specimen A4: (a) Force-displacement curve with annotations, (b) early edge crack, (c) nucleation of crack, and (d) crack propagation.

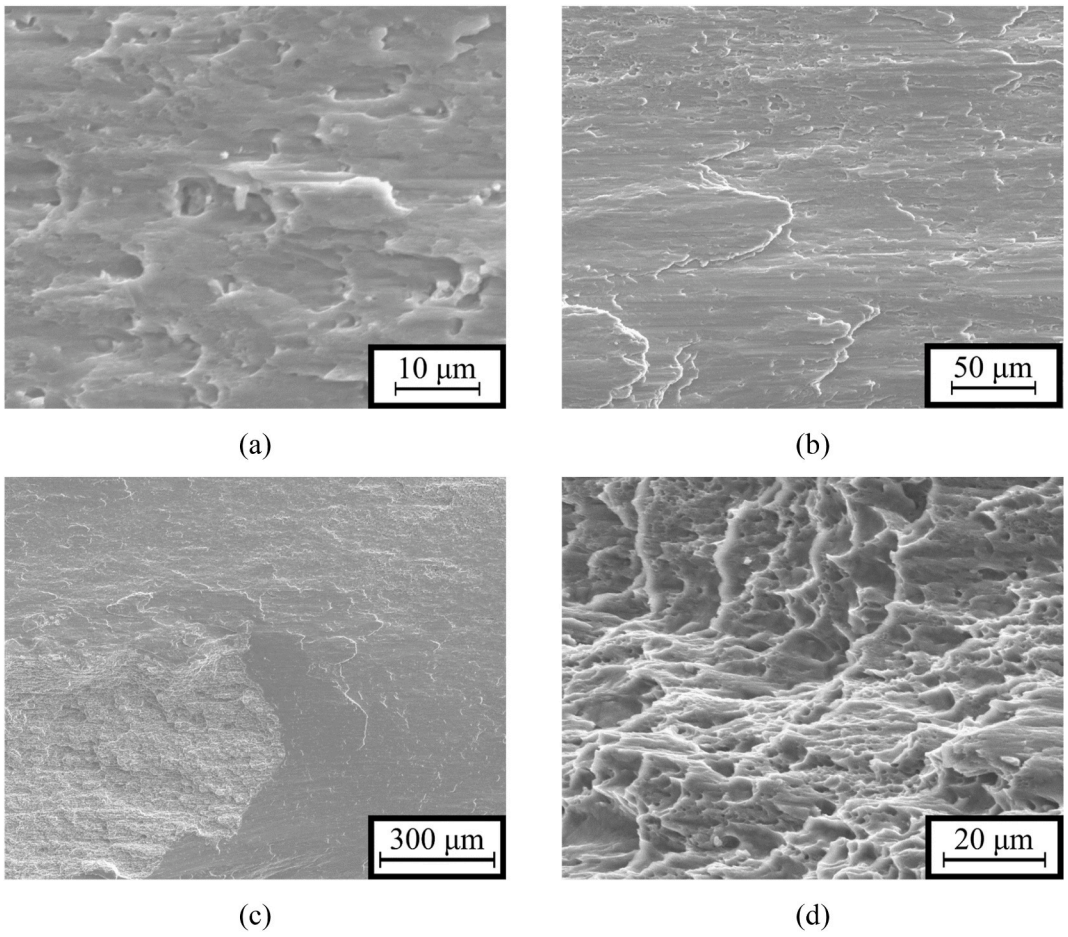

Fig. 15. SEM images showing typical features of the fracture surfaces: (a) ripple-like shear surface (B6), (b) flat shear surface (B6), (c) flat shear surface interrupted by a zone of dimples (B6), and (d) slanted dimples at the edge of the specimen (A6).

displays the fracture surface inside the bulk of the specimen and between the edge and the highly strained zone. The fracture surface consists of flat areas, slightly ripple-like, with scattered small shallow, almost flat, dimples. Fig. 15b reveals the fracture surface at or near the left side of the highly strained zone. The lower half of the image was captured at the surface of the notch root and is typical for the entire central part of the fracture surface. The image displays large smooth flat areas. Towards the middle of the specimen, at the edge, several dimpled areas are visible. One of these areas is shown in the lower left side of Fig. 15c. The dimpled area is associated with sections of the specimen which did not fracture until after the removal of the specimens from the testing machine. Several specimens were not completely split in two after testing due to small sections at the edges that were still attached, and the dimpled surface arose due to the damage caused in the separation process. The likely course of events for the specimens which fail due to crack initiation in the highly strained zone is as follows:

- a shear crack is nucleated at the surface in the highly strained zone,
- the nucleated surface crack propagates into the bulk of the gauge region,
- the through-thickness crack then propagates in the length direction of the gauge region, and ultimately causes fracture as the crack reach the edges.

Fig. 15d shows the somewhat elongated dimpled surface at the fracture initiation site of specimen A6, which fractured due to the propagation of an edge crack. The dimpled surface is typically associated with ductile fracture, and the surface bears evidence that a mixed mode of ductile void growth and shearing is present.

4. Conclusions

In-plane shear tests were conducted on two extruded 6000-series aluminium alloys in temper T6 in two material directions. The two alloys have different area fractions of constituent particles while having similar grain structure, crystallographic texture, strength, and work hardening. An experimental-numerical approach was used to determine the stress and strain fields at failure, which involved digital image correlation and crystal plasticity finite element analysis. Crack paths were determined by visual inspection of digital images captured during testing and fractography was conducted on four representative specimens.

The following conclusions can be drawn based on the experimental and numerical results:

- The alloy with the high area fraction of constituent particles has markedly lower average shear strain at failure and the difference in the failure strain between the two alloys is larger for loading along the transverse direction than along the extrusion direction.
- While the average shear strain at failure is similar in the two load cases for the alloy with the high particle fraction, it is significantly larger in the transverse direction for the alloy with the lower particle fraction.

- For the alloy with the high particle fraction, fracture consistently initiated within the highly strain area of the gauge section, while for the other alloy, fracture initiated at the edge in some specimens.
- The fracture surfaces display features typically associated with shear damage and together with the assessment of the crack path provide credible evidence that most of the specimens for both alloys fractured due to shear damage.
- The CP-FEM simulations predicted the force and average shear strain against the displacement and the local strain fields within the groove of the specimen with good accuracy, even if the force level was somewhat underestimated.
- No significant failure anisotropy was observed at the macroscopic level for alloy B, while the numerical results indicate failure anisotropy at a microscopic level.
- Severe texture evolution was observed in the CP-FEM simulations, and the resulting crystallographic texture was dependent upon the direction of straining. This finding underlines the importance of accounting for texture evolution in the modelling of materials subjected to large deformations in shear.

CRediT authorship contribution statement

Asle Joachim Tomstad: Conceptualization, Formal analysis, Investigation, Writing – original draft, Writing – review & editing, Visualization. **Bjørn Håkon Frodal:** Software, Formal analysis, Data curation, Writing – original draft, Writing – review & editing. **Tore Børvik:** Conceptualization, Writing – original draft, Writing – review & editing, Supervision. **Odd Sture Hopperstad:** Conceptualization, Writing – original draft, Writing – review & editing, Supervision.

Declaration of competing interest

The authors declare that they have no known competing financial interests or personal relationships that could have appeared to influence the work reported in this paper.

Data availability

The raw/processed data required to reproduce the findings in this study cannot currently be shared as the data also forms part of several ongoing studies. However, the data may be made available from the corresponding author upon request.

Acknowledgments

The authors gratefully appreciate the financial support from NTNU, and the Research Council of Norway through the FRIPRO Program FractAl, Project No. 250553. Further, the authors express their gratitude towards Dr. Susanne Thomesen for conducting the fractography in the SEM. The authors would like to thank Dr. Afaf Saai and Mr. Jon Troset for designing and constructing the shear device.

Appendix

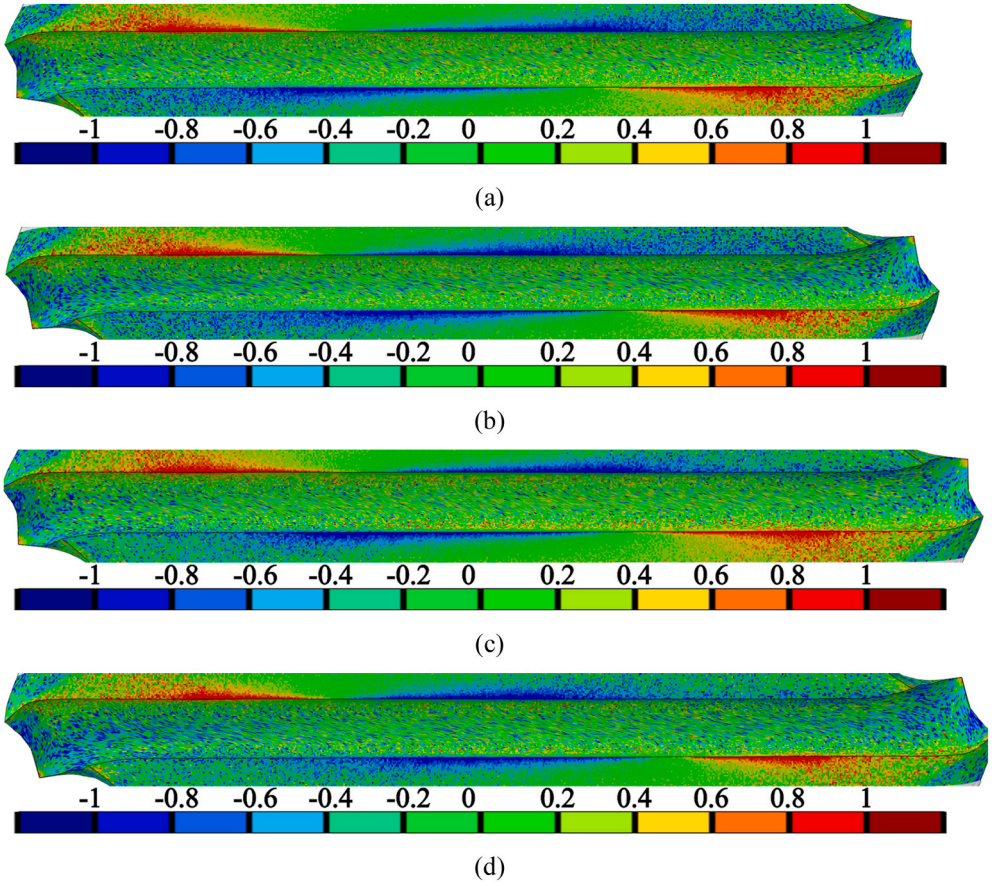

Fig. A1. Distribution of the Lode parameter on the surface of the groove at failure: (a) B7 (ED), (b) A7 (ED), (c) B4 (TD), and (d) A3 (TD).

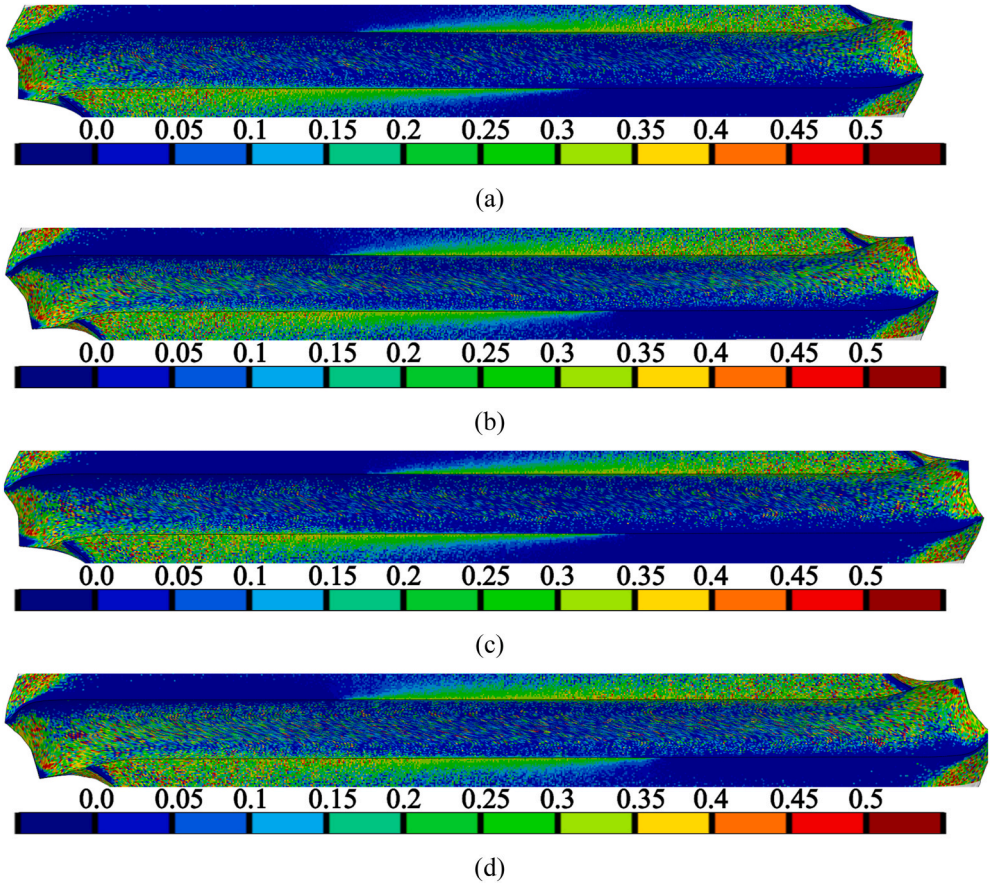

Fig. A2. Distribution of the stress triaxiality on the surface of the groove at failure: (a) B7 (ED), (b) A7 (ED), (c) B4 (TD), and (d) A3 (TD).

References

[1] A.A. Benzerga, J.B. Leblond, Ductile fracture by void growth to coalescence, Adv. Appl. Mech. 44 (2010) 169–305.
[2] A. Pineau, A.A. Benzerga, T. Pardoen, Failure of metals I: Brittle and ductile fracture, Acta Mater. 107 (2016) 424–483.
[3] J.R. Rice, D.M. Tracy, On the ductile enlargement of voids in triaxial stress fields, J. Mech. Phys. Solid. 17 (1969) 201–217.
[4] H. Agarwal, A.M. Gokhale, S. Graham, M.F. Horstemeyer, Void growth in 6061-aluminum alloy under triaxial stress state, Mater. Sci. Eng., A 341 (2003) 35–42.
[5] F.M. Beremin, Cavity formation from inclusions in ductile fracture of A508 steel, Metall. Trans. A 12 (1981) 723–731.
[6] M. Achouri, G. Germain, P. Dal Santo, D. Saidane, Experimental characterization and numerical modeling of micromechanical damage under different stress states, Mater. Des. 50 (2013) 207–222.
[7] A.A. Benzerga, J. Besson, A. Pineau, Anisotropic ductile fracture: Part I: experiments, Acta Mater. 52 (2004) 4623–4638.
[8] L. Babout, W. Ludwig, E. Maire, J.Y. Buffière, Damage assessment in metallic structural materials using high resolution synchrotron X-ray tomography, Nucl. Instrum. Methods Phys. Res. Sect. B Beam Interact. Mater. Atoms 200 (2003) 303–307.
[9] A. Weck, D.S. Wilkinson, E. Maire, H. Toda, Visualization by X-ray tomography of void growth and coalescence leading to fracture in model materials, Acta Mater. 56 (2008) 2919–2928.
[10] A. Weck, D.S. Wilkinson, Experimental investigation of void coalescence in metallic sheets containing laser drilled holes, Acta Mater. 56 (2008) 1774–1784.
[11] I. Barsoum, J. Faleskog, Rupture mechanisms in combined tension and shear – Experiments, Int. J. Solid Struct. 44 (2007) 1768–1786.
[12] J. Faleskog, I. Barsoum, Tension–torsion fracture experiments—Part I: experiments and a procedure to evaluate the equivalent plastic strain, Int. J. Solid Struct. 50 (2013) 4241–4257.
[13] J. Papasidero, V. Doquet, D. Mohr, Determination of the effect of stress state on the onset of ductile fracture through tension-torsion experiments, Exp. Mech. 54 (2014) 137–151.
[14] J. Papasidero, V. Doquet, D. Mohr, Ductile fracture of aluminum 2024-T351 under proportional and non-proportional multi-axial loading: Bao–Wierzbicki results revisited, Int. J. Solid Struct. 69–70 (2015) 459–474.
[15] A.J. Tomstad, M. Boåsen, J. Faleskog, T. Børvik, O.S. Hopperstad, On the Influence of Stress State on Ductile Fracture of Two 6000-series Aluminium Alloys with Different Particle Content, To be submitted for possible journal publication, 2022.
[16] A. Ghahremaninezhad, K. Ravi-Chandar, Ductile failure behavior of polycrystalline Al 6061-T6 under shear dominant loading, Int. J. Fract. 180 (2013) 23–39.
[17] D. Achani, O.G. Lademo, O. Engler, O.S. Hopperstad, Evaluation of constitutive models for textured aluminium alloys using plane-strain tension and shear tests, Int. J. Material Form. 4 (2011) 227–241.
[18] M. Luo, M. Dunand, D. Mohr, Experiments and modeling of anisotropic aluminum extrusions under multi-axial loading – Part II: ductile fracture, Int. J. Plast. 32–33 (2012) 36–58.
[19] M. Fourmeau, T. Børvik, A. Benallal, O.S. Hopperstad, Anisotropic failure modes of high-strength aluminium alloy under various stress states, Int. J. Plast. 48 (2013) 34–53.
[20] Y. Lou, J.W. Yoon, Anisotropic behavior in plasticity and ductile fracture of an aluminum alloy, Key Eng. Mater. 651–653 (2015) 163–168.
[21] Y. Lou, J.W. Yoon, Anisotropic ductile fracture criterion based on linear transformation, Int. J. Plast. 93 (2017) 3–25.
[22] Y. Lou, J.W. Yoon, Alternative approach to model ductile fracture by incorporating anisotropic yield function, Int. J. Solid Struct. 164 (2019) 12–24.
[23] C.C. Roth, T.F. Morgeneyer, Y. Cheng, L. Helfen, D. Mohr, Ductile damage mechanism under shear-dominated loading: in-situ tomography experiments on dual phase steel and localization analysis, Int. J. Plast. 109 (2018) 169–192.
[24] T. Tancogne-Dejean, C.C. Roth, T.F. Morgeneyer, L. Helfen, D. Mohr, Ductile damage of AA2024-T3 under shear loading: mechanism analysis through in-situ laminography, Acta Mater. 205 (2021), 116556.
[25] F. Hannard, A. Simar, E. Maire, T. Pardoen, Quantitative assessment of the impact of second phase particle arrangement on damage and fracture anisotropy, Acta Mater. 148 (2018) 456–466.
[26] F. Hannard, S. Castin, E. Maire, R. Mokso, T. Pardoen, A. Simar, Ductilization of aluminium alloy 6056 by friction stir processing, Acta Mater. 130 (2017) 121–136.
[27] B. Kondori, T.F. Morgeneyer, L. Helfen, A.A. Benzerga, Void growth and coalescence in a magnesium alloy studied by synchrotron radiation laminography, Acta Mater. 155 (2018) 80–94.
[28] A.J. Tomstad, S. Thomesen, T. Børvik, O.S. Hopperstad, Effects of constituent particle content on ductile fracture in isotropic and anisotropic 6000-series aluminium alloys, Mater. Sci. Eng., A 820 (2021), 141420.

[29] V. Tarigopula, O.S. Hopperstad, M. Langseth, A.H. Clausen, F. Hild, O.G. Lademo, M. Eriksson, A study of large plastic deformations in dual phase steel using digital image correlation and FE analysis, Exp. Mech. 48 (2008) 181–196.
[30] G. Gruben, E. Fagerholt, O.S. Hopperstad, T. Børvik, M. Langseth, Numerical simulation of ductile fracture in modified Arcan test, Proc. Mater. Sci. 3 (2014) 661–666.
[31] S. Thomesen, Plastic Flow and Fracture of Isotropic and Anisotropic 6000-series Aluminium Alloys: Experiments and Numerical Simulations, Ph.D. thesis. NTNU - Norwegian University of Science and Technology, Trondheim, Norway, 2019.
[32] S. Thomesen, O.S. Hopperstad, T. Børvik, Anisotropic plasticity and fracture of three 6000-series aluminium alloys, Metals 11 (2021) 557.
[33] O. Engler, V. Randle, Introduction to Texture Analysis: Macrotexture, Microtexture, and Orientation Mapping, second ed., CRC press, Taylor & Francis Group, 2010.
[34] B.H. Frodal, K.O. Pedersen, T. Børvik, O.S. Hopperstad, Influence of pre-compression on the ductility of AA6xxx aluminium alloys, Int. J. Fract. 206 (2017) 131–149.
[35] D. Degenhardt, L. Greve, M. Andres, T.K. Eller, J. Copik, P. Horst, Simplified temperature-dependent elasto-viscoplastic deformation and fracture modeling of a talcum-filled PP/PE co-polymer, Int. J. Plast. 119 (2019) 291–312.
[36] cited, https://www.ntnu.edu/kt/ecorr. (Accessed 22 February 2022).
[37] Abaqus, Version 2019. Dassault Systemès Simulia Corporation. Providence, Rhode Island, USA, 2019.
[38] B.H. Frodal, L.E.B. Dæhli, T. Børvik, O.S. Hopperstad, Modelling and simulation of ductile failure in textured aluminium alloys subjected to compression-tension loading, Int. J. Plast. 118 (2019) 36–69.
[39] B.H. Frodal, S. Thomesen, T. Børvik, O.S. Hopperstad, On the coupling of damage and single crystal plasticity for ductile polycrystalline materials, Int. J. Plast. 142 (2019), 102996.
[40] C.C. Roth, D. Mohr, Determining the strain to fracture for simple shear for a wide range of sheet metals, Int. J. Mech. Sci. 149 (2018) 224–240.